

Spray-Coated Lead-Free $\text{Cs}_2\text{AgBiBr}_6$ Double Perovskite Solar Cells with High Open-Circuit Voltage

Nathan Daem, Jennifer Dewalque, Felix Lang, Anthony Maho, Gilles Spronck, Catherine Henrist, Pierre Colson, Samuel D. Stranks, and Rudi Cloots*

Lead-free $\text{Cs}_2\text{AgBiBr}_6$ double perovskite is considered a promising alternative photovoltaic absorber to the widely used lead halide perovskite due to its easy processability, high stability, and reduced toxicity. Herein, for the first time spray processing for the deposition of $\text{Cs}_2\text{AgBiBr}_6$ double perovskite thin films is reported. Microstructural (X-ray diffraction, scanning electron microscopy) and optoelectronic (absorbance, photoluminescence, photocurrent density versus applied voltage curves, electrochemical impedance spectroscopy) properties of spray-coated film are compared with the spin-coated benchmark. Incorporation of the spray-coated $\text{Cs}_2\text{AgBiBr}_6$ double perovskite thin films in solar cells leads to a 2.3% photoconversion efficiency with high open-circuit voltage of 1.09 V. This study highlights the suitability of ultrasonic spray deposition for the optimization of $\text{Cs}_2\text{AgBiBr}_6$ solar cells in terms of light absorption properties and charge transfer at the $\text{Cs}_2\text{AgBiBr}_6$ /hole transporting layer interface.

coefficients, high charge carrier mobilities, and long charge carrier diffusion lengths.^[1–4] With power conversion efficiencies (PCEs) exceeding 25%,^[5] these cost-efficient materials constitute strong alternatives to commonly used Si-based solar cells.^[6] However, lead toxicity and poor stability over time are significant obstacles toward their use and commercialization.^[7,8] This is why many research groups focus—through theoretical and/or experimental studies—on the development of lead-free perovskite materials.^[9–15] To diminish the amount of lead in perovskite PV absorber, two options are generally envisaged: the first is to replace a fraction of lead by a non-hazardous metal cation; the second is to completely substitute lead by a nontoxic element such as Ge(II),

1. Introduction

Since 2009, inorganic–organic lead halide perovskites have been widely studied in the field of photovoltaics (PV) for their excellent physical and optical properties, including high extinction

Mn(II), Cu(II), Bi(III), or Sb(III).^[10]

Lead-free halide double perovskites are considered as one of the promising PV absorber alternatives to lead halide perovskite in view of their nontoxic character and long-term stability.^[14] The double perovskite crystal structure $\text{A}_2\text{B}^{'+}\text{B}^{''3+}\text{X}_6$ (where A and B' are monovalent ions, B'' is a trivalent metal, and X is an halide) is an expansion of the ABX_3 perovskite crystal lattice, where two Pb^{2+} on B sites are replaced by one monovalent ion B^{+} and one trivalent ion $\text{B}^{''3+}$.^[16] Double perovskite materials were first reported during the 1970s but, to date, the optoelectronic properties of only a few formulations (namely, $\text{Cs}_2\text{NaBiX}_6$ and $\text{Cs}_2\text{AgBiX}_6$)—with more adapted properties for solar cells—have been studied in PV devices.^[16–30] $\text{Cs}_2\text{AgBiBr}_6$ has an indirect bandgap of 1.95 eV and a direct bandgap of 2.20 eV, which makes the material particularly interesting as wide-gap semiconductor top cell in tandem or even triple junction solar cells.^[31]

Greul et al. first reported $\text{Cs}_2\text{AgBiBr}_6$ films in solar cells.^[21] A PCE of 2.4% (short-circuit current density: $J_{\text{sc}} = 3.93 \text{ mA cm}^{-2}$; open-circuit voltage: $V_{\text{oc}} = 0.98 \text{ V}$, fill factor (FF) = 0.63) was reached using an n–i–p configuration comprising: FTO glass/compact (c)- TiO_2 /mesoporous (mp)- TiO_2 / $\text{Cs}_2\text{AgBiBr}_6$ /Spiro-OMeTAD/Au. Here, they spin-coated the films from a solution containing the three mixed precursors (CsBr , AgBr , and BiBr_3) dissolved in dimethylsulfoxide (DMSO). By contrast, most studies first prepare $\text{Cs}_2\text{AgBiBr}_6$ powder^[16–20]—by reaction of CsBr , AgBr , and BiBr_3 in HBr at 120 °C for 2 h—which then is further dissolved in DMSO for thin film deposition. However, the resulting solar cells exhibit low PCE values between 1.1% and 2.5 % while being time-consuming in terms of photoactive layer

N. Daem, J. Dewalque, A. Maho, G. Spronck, C. Henrist, P. Colson, R. Cloots

Group of Research in Energy and Environment from Materials (GREENMAT)

CESAM Research Unit

Chemistry Department

University of Liege

B-4000 Liege, Belgium

E-mail: rcloots@uliege.be

F. Lang, S. D. Stranks

Cavendish Laboratory

Department of Physics

University of Cambridge


CB3 0HE Cambridge, UK

S. D. Stranks

Department of Chemical Engineering & Biotechnology

University of Cambridge

CB3 0AS Cambridge, UK

 The ORCID identification number(s) for the author(s) of this article can be found under <https://doi.org/10.1002/solr.202100422>.

© 2021 The Authors. Solar RRL published by Wiley-VCH GmbH. This is an open access article under the terms of the Creative Commons Attribution License, which permits use, distribution and reproduction in any medium, provided the original work is properly cited.

DOI: 10.1002/solr.202100422

preparation. Some groups have also reported the deposition of $\text{Cs}_2\text{AgBiBr}_6$ by thermal evaporation with 1.4% PCE.^[16,25,27]

Up to now, the best PCE of $\text{Cs}_2\text{AgBiBr}_6$ -based solar cells reached 2.8% through the engineering of multifunctional dye interlayers^[23] or the incorporation of single-layered MXene nano-sheets into titania ($\text{Ti}_3\text{C}_2\text{T}_x/\text{TiO}_2$) as a multifunctional electron transport layer (ETL).^[30] Apart from interlayer design and ETL engineering, it has also been shown that the film processing itself strongly influences the optoelectronic properties of the photoactive layers in classical lead halide perovskites solar cells.^[16,19,32,33] The thin film processing must also matter for microstructural and optoelectronic properties of $\text{Cs}_2\text{AgBiBr}_6$ -based solar cells.

In our study, we deposited $\text{Cs}_2\text{AgBiBr}_6$ double perovskite thin films by ultrasonic spray and compared results with the spin-coated benchmark. Ultrasonic spray deposition has been shown to be very effective for inorganic–organic lead halide perovskites solar cell manufacturing, with a record PCE of $\approx 20\%$ on small area substrates.^[34] Due to the production of micron-sized droplets by piezoelectric transducers, ultrasonic spray deposition allows the deposition of very uniform lead halide perovskite thin films with smaller average grain size in comparison with spin-coated films.^[35] In addition, ultrasonic spray deposition is a scalable, semiautomated, atmospheric pressure process. In this article, we used ultrasonic spray deposition to process $\text{Cs}_2\text{AgBiBr}_6$ double perovskite thin films. Spray deposition allows the formation of very smooth, uniform, and pinhole-free layers, with smaller and better connected grains compared with the spin-coated benchmark. The corresponding spray-coated devices reached 2.3% efficiency, one of the best performances for spin-coated benchmarks to date. Such performance was directly attributed to the improvement of the $\text{Cs}_2\text{AgBiBr}_6$ interface induced by the spray deposition process and the improvement of the $\text{Cs}_2\text{AgBiBr}_6$ /Spiro-OMeTAD interface. As a consequence of the interface optimization, spray-coated devices led to an impressively high V_{oc} of 1.09 V compared with 0.82 V for the spin-coated benchmark, just surpassing the V_{oc} record for a solution-processed $\text{Cs}_2\text{AgBiBr}_6$ double perovskite layer.

2. Results and Discussion

2.1. Structure and Morphology of $\text{Cs}_2\text{AgBiBr}_6$ Thin Films

Prior to solar cell assembly, X-ray diffraction (XRD) measurements were performed on spin-coated and spray-coated $\text{Cs}_2\text{AgBiBr}_6$ films to confirm the synthesis of phase-pure films. $\text{Cs}_3\text{Bi}_2\text{Br}_9$ (reflection at 12.8° and 30.9°) and AgBr (reflection at 44.2°) are two undesired side phases that can be formed during the film deposition.^[21] To avoid such side phases formation, an annealing temperature above 250°C was required (best conditions: 285°C) for the complete conversion of the precursors into the desired $\text{Cs}_2\text{AgBiBr}_6$ double perovskite crystal phase.^[21] **Figure 1** shows the XRD patterns of the $\text{Cs}_2\text{AgBiBr}_6$ double perovskite deposited by spin-coating and spray-coating on mp-TiO₂/c-TiO₂/FTO glass substrates. Three main peaks at 15.7° , 22.5° , and 31.8° were observed, representative of the (200), (220), and (400) reflections of the $\text{Cs}_2\text{AgBiBr}_6$ (JCPDS file number: 01-084-8699) double perovskite, respectively, along with (100), (311), (222), and (331) reflections at 13.7° , 26.5° , 27.5° , and 35.7° , respectively. Specific reflections of residual $\text{Cs}_3\text{Bi}_2\text{Br}_9$ or

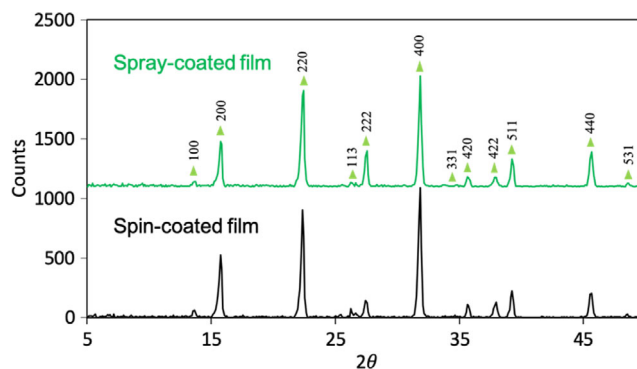


Figure 1. X-ray diffractograms of spin-coated (black) and spray-coated (green) $\text{Cs}_2\text{AgBiBr}_6$ films (after thermal treatment).

AgBr were not observed. $\text{Cs}_2\text{AgBiBr}_6$ average crystallite size was calculated from Scherrer equation on the (400) peak signal. No significant difference was observed between spin-coated and spray-coated samples, with 28 and 34 nm average values extracted, respectively.

The morphology of the $\text{Cs}_2\text{AgBiBr}_6$ double perovskite films was evaluated by scanning electron microscopy (SEM) analysis. For the spin-coated benchmark (**Figure 2a–c**), ≈ 350 nm diameter grains were observed on top of the mp-TiO₂ layer, with a poorly connected $\text{Cs}_2\text{AgBiBr}_6$ network. Ultrasonic spray deposition (**Figure 2d–f**) allowed for the formation of a very smooth and uniform $\text{Cs}_2\text{AgBiBr}_6$ film with smaller grains (≈ 150 nm), as previously observed for ultrasonic spray-processed lead halide perovskite compared with a spin-coated counterpart.^[35] In the literature, density functional theory (DFT) calculations determined the spectroscopic limited maximum efficiency (SLME) of $\text{Cs}_2\text{AgBiBr}_6$, which is 7.92% for a 200 nm-thick film.^[36] Thicker overlayers would result in increased recombination due to the limited diffusion length of electrons, without significant enhancement of light absorption. The strength of optical absorption and the nature of the bandgap influence the SLME.^[17] By adjusting the concentration of the spin-coated and spray-coated solutions, an average overlayer of 200 nm thickness was obtained for both samples. However, there were more variations in spin-coated films due to its higher roughness (**Figure 2c** and S3, Supporting Information).

2.2. Optical Properties of $\text{Cs}_2\text{AgBiBr}_6$ Thin Films

The optical absorbance curves of the spin-coated and spray-coated $\text{Cs}_2\text{AgBiBr}_6$ thin films are shown in **Figure 3a**. A strong absorption peak is present at an ≈ 440 nm wavelength, as previously observed for $\text{Cs}_2\text{AgBiBr}_6$ and other double perovskite materials such as $\text{Cs}_3\text{Bi}_2\text{I}_9$.^[19] However, the origin of this peak is still not very clear;^[37] it could be associated with trapped excitonic transitions^[38] or even color centers in the material.^[39] The absorbance is globally higher for the spray-coated film than the spin-coated benchmark, but this is attributed to less uniform thickness for spin-coated films as seen in cross-sectional images (**Figure 2c** and S3, Supporting Information). Tauc plots (**Figure 3b**) allow for the determination of a direct band gap of ≈ 2.20 and ≈ 2.30 eV, respectively, for spray-coated and

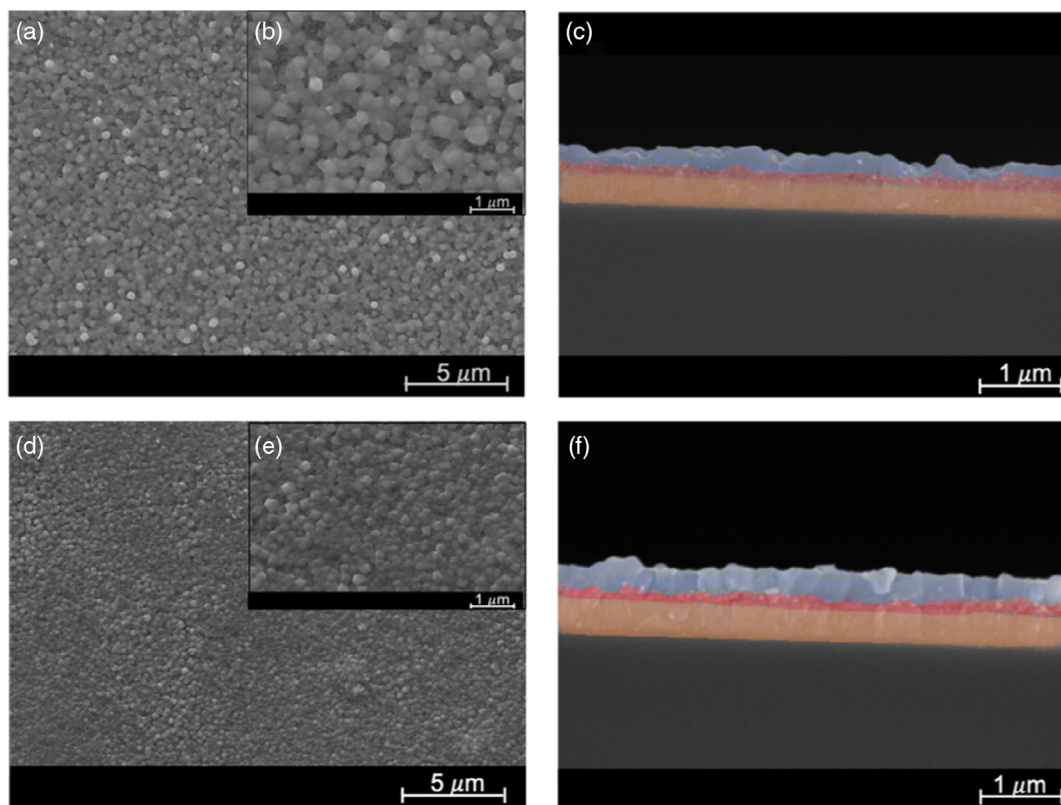


Figure 2. SEM micrographs (top-view [left row] and cross section [right row]) of a–c) spin-coated and d–f) spray-coated $\text{Cs}_2\text{AgBiBr}_6$ films with the following architecture: glass (dark grey)/FTO (orange)/c- TiO_2 and mp- TiO_2 (red) infiltrated by $\text{Cs}_2\text{AgBiBr}_6/\text{Cs}_2\text{AgBiBr}_6$ overlayer (blue).

spin-coated samples. The bandgaps determined for the spray-coated and spin-coated samples are in accordance with values previously reported in the literature for similar synthesis conditions.^[20,40] These absorbance data highlight the strong interest in ultrasonic spray-coating to improve the $\text{Cs}_2\text{AgBiBr}_6$ films morphology and structures and therefore their photoabsorbing properties, which is of strong importance for PV purposes.

The photoluminescence (PL) spectra of the spray-coated and spin-coated $\text{Cs}_2\text{AgBiBr}_6$ films are shown in **Figure 4a**. Most importantly, the PL emission is broad and centered around 645 nm (≈ 1.9 eV) for both samples, which is attributed to the indirect bandgap of about 1.9 eV,^[40] without significant contribution from the direct bandgap around 560 nm (2.2 eV). The PL spectra shown in **Figure 4a** are therefore dominated by recombination through the indirect gap, though recent low-temperature studies suggest that PL emission might arise from color centers in $\text{Cs}_2\text{AgBiBr}_6$ rather than band-to-band transitions.^[39] The PL peak intensity for the spray-coated film is higher than for the spin-coated benchmark. An increase in PL intensity is usually attributed to a reduced number of defect sites or less active defect sites responsible for trap-assisted recombination.^[37] However, the higher PL intensity can be explained by the more continuous layer for spray-coated film and so the more absorption of excitation light too. **Figure 4b** shows a PL image with high spatial resolution confirming the more uniform and smooth spray-coated film compared with the less connected spin-coated network. Indeed, the PL intensity is higher in each area with a better

homogeneity on the microscale for spray-coated film and the distribution is a little broader for spin-coated film compared with spray-coated film (**Figure S4**, Supporting Information). We further note that zoomed-out PL images (**Figure S5**, Supporting Information) reveal inhomogeneities on larger length scales that we attribute to thickness fluctuations across longer distances across the film. To complement our steady-state PL characterization, we recorded the PL decay kinetics of the two films (**Figure S6**, Supporting Information). However, we cannot observe significant difference between the two films.

2.3. Assembly and Characterization of $\text{Cs}_2\text{AgBiBr}_6$ Double Perovskite Solar Cells

The PV performance of the $\text{Cs}_2\text{AgBiBr}_6$ films prepared by spin-coating or ultrasonic spray deposition is evaluated in PV devices with the following architecture: FTO glass/c- TiO_2 /mp- $\text{TiO}_2/\text{Cs}_2\text{AgBiBr}_6$ /Spiro-OMeTAD/Au (**Figure S2** and **S3**, Supporting Information). As shown in **Figure 5**, the cells exhibit a very low hysteresis. The champion spin-coated and spray-coated devices present PCEs of 2.3% (**Table 1**). The PCEs reported in this work are among the highest efficiencies reached to date, which is noted given it is achieved using a highly processable ultrasonic spray deposition technique for the preparation of $\text{Cs}_2\text{AgBiBr}_6$ -based solar cells. As expected from PL results, the spray-coated $\text{Cs}_2\text{AgBiBr}_6$ device shows V_{oc}

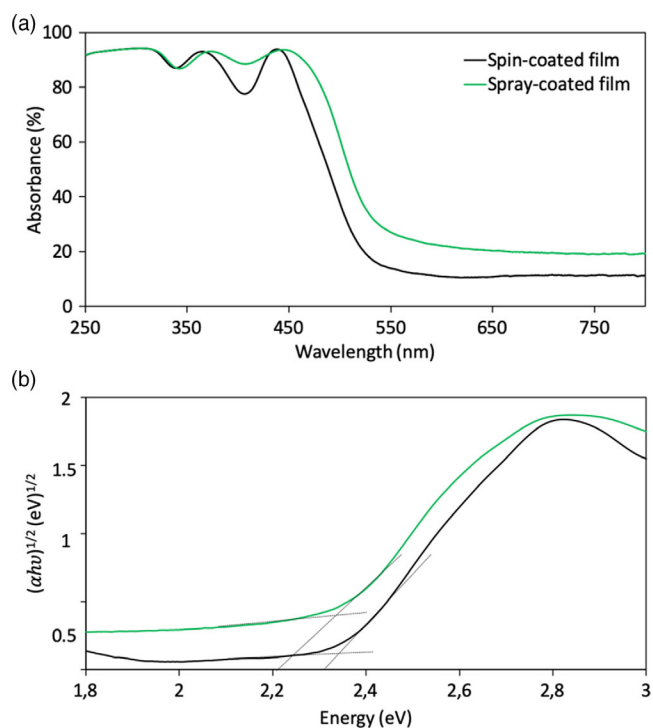


Figure 3. a) Absorbance spectra and b) Tauc plots (dashed lines: direct band gap estimation) of spin-coated (black) and spray-coated (green) $\text{Cs}_2\text{AgBiBr}_6$ films.

enhancement (1.09 vs 0.82 V for the spin-coated benchmark). Indeed, the more uniform and covering spray-coated films lead to lowered recombination in spray-coated devices. Fewer electrons are trapped in the intermediate energy levels, which further results in the increased open-circuit potential. This V_{oc} value of 1.09 V is so far the highest reported for $\text{Cs}_2\text{AgBiBr}_6$ -based solar cells with a solution process; only a higher V_{oc} (1.12 V) was obtained by sequential vapor deposition.^[25] Yan et al. were the first to exceed 1 V for direct and reverse measures ($V_{oc} = 1.02$ and 1.06 V, respectively) by using a spin-coated dye interlayer to suppress the carrier recombination among others.^[23] In our study, ultrasonic spray process allows for the significant improvement of the open-circuit voltage for direct and reverse measures, without additional interlayer engineering. We therefore demonstrate that the processing method used for the deposition of the $\text{Cs}_2\text{AgBiBr}_6$ photoactive layer strongly influences its charge transfer properties. Despite the higher absorbance and the better connectivity (Figure 2d and 3a) of the $\text{Cs}_2\text{AgBiBr}_6$ grains in the photoactive layer, the spray-coated device shows reduced current density (J_{sc}) compared with the spin-coated benchmark and this trend is corroborated by the external quantum efficiency (EQE) measurements (Figure S8, Supporting Information). The same conclusions can be drawn on average PV parameters (Figure S7, Supporting Information, 20 devices average). The difference between champion and others devices comes from reduced average J_{sc} . Indeed, others parameters (V_{oc} and FF) are similar.

To further analyze the charge transfer properties of spin-coated and spray-coated $\text{Cs}_2\text{AgBiBr}_6$ -based solar cells,

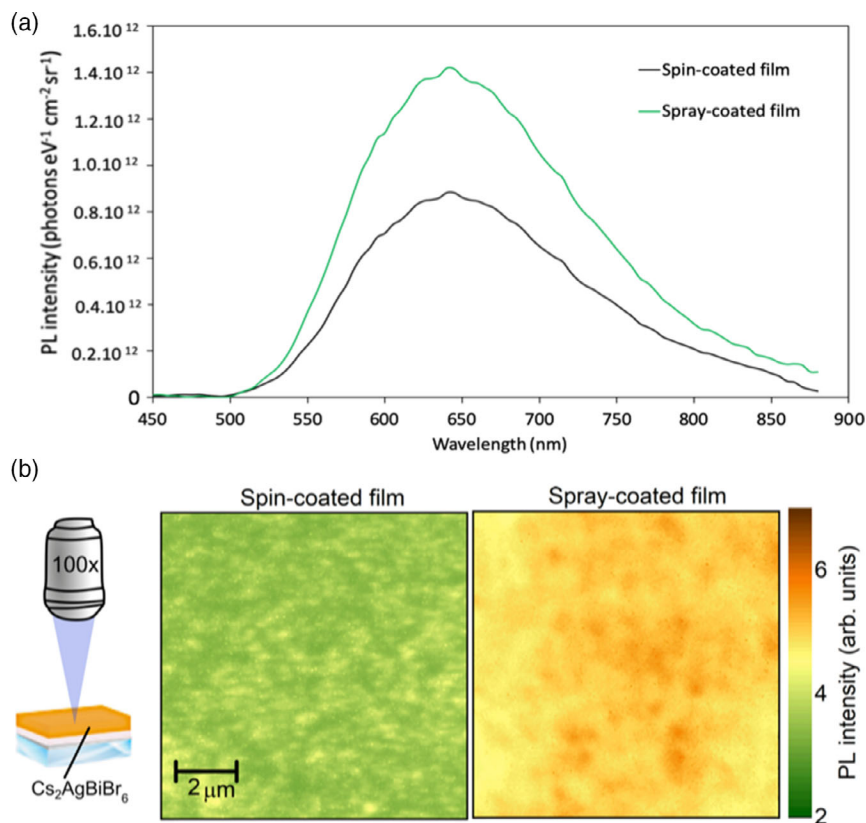


Figure 4. a) Steady-state PL and b) PL images of spin-coated and spray-coated $\text{Cs}_2\text{AgBiBr}_6$ films recorded with 100 \times objective.

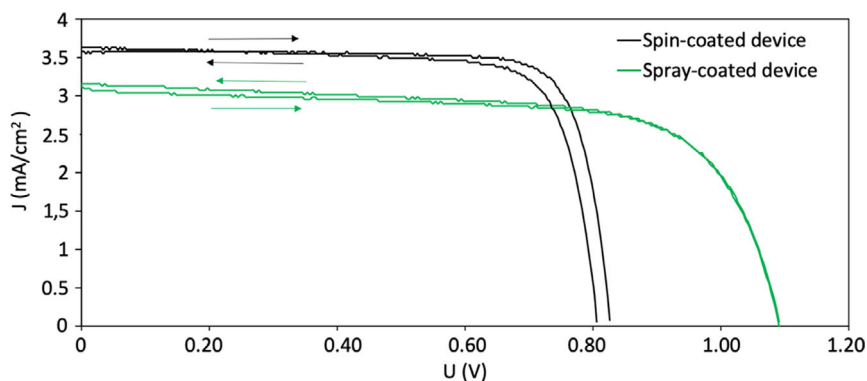


Figure 5. a) J – V curves of champion spin-coated (black) and spray-coated (green) $\text{Cs}_2\text{AgBiBr}_6$ -based solar cells.

Table 1. Photovoltaic parameters of the champion spin-coated and spray-coated $\text{Cs}_2\text{AgBiBr}_6$ -based solar cells.

		V_{oc} [V]	J_{sc} [mA cm^{-2}]	FF	PCE [%]
Spin-coated device	Direct	0.827	3.6	81	2.3
	Reverse	0.811	3.7	78	2.3
Spray-coated device	Direct	1.091	3.1	70	2.3
	Reverse	1.093	3.2	68	2.3

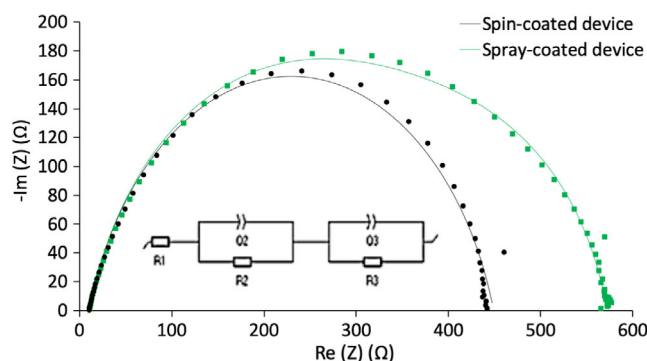


Figure 6. EIS Nyquist plots of spin-coated (black) and spray-coated (green) $\text{Cs}_2\text{AgBiBr}_6$ -based solar cells; inset: equivalent electrical circuit used for data fitting.

electrochemical impedance spectroscopy (EIS) is conducted. EIS results are presented as Nyquist plots in **Figure 6**. Data were fitted with the equivalent circuit model shown in the inset^[41] and are shown in **Table 2**. The equivalent electrical circuit consists of: an R_1 resistance associated with wires and contacts (high frequency); an $R_2//Q_2$ element (with Q as constant phase element

modeling an imperfect capacitor) characteristic of the selective contacts, including c-TiO_2 and mp-TiO_2 for electron-selective contacts and the Spiro-OMeTAD for hole-selective contacts, respectively (medium frequency); and an $R_3//Q_3$ element for interfacial recombination between electrons and holes (low frequency). From data fitting (**Table 2**), the interfacial recombination resistance R_3 of the spray-coated device is 367.1Ω , which is higher than R_3 value of the spin-coated device (254.4Ω). As the recombination rate at the $\text{Cs}_2\text{AgBiBr}_6$ /Spiro-OMeTAD interface is inversely proportional to R_3 , it reveals faster interfacial recombination in the spin-coated device. Therefore, it can be assumed that charge transfer at the $\text{Cs}_2\text{AgBiBr}_6$ /Spiro-OMeTAD interface is improved in the spray-coated device. This is in agreement with V_{oc} values obtained for both devices: high interfacial recombination increases the forward bias diffusion current, which, in turn, reduces the open-circuit voltage.^[42] Looking at R_2 selective contacts resistance, we determine lower R_2 value for the spin-coated device (177.7Ω) compared with the spray-coated device (191.2Ω), corresponding to more efficient charge transfer into the selective contact for the spin-coated device. Because of the centrifugal force inherent in the deposition process, spin-coating can allow for a better infiltration of $\text{Cs}_2\text{AgBiBr}_6$ within the mp-TiO_2 layer, leading to improved charge collection at the electron selective contact and thus increased J_{sc} . Moreover, the larger grains reported for the spin-coated sample reduce the amount of grain boundaries and so a decrease in the recombination rate is expected. The EIS data thus corroborate PL and J – V results.

3. Conclusion

$\text{Cs}_2\text{AgBiBr}_6$ double perovskite is considered as a promising lead-free alternative to commonly used lead halide perovskites for solar cell applications, due to its easy processability, high

Table 2. Resistance (R) and constant phase element (Q) fitting parameters obtained from EIS data measured on the spin-coated and spray-coated $\text{Cs}_2\text{AgBiBr}_6$ -based solar cells.

	R_1 [Ω]	Q_2 [$10^{-6} \text{ F s}^{a-1}$]	a	R_2 [Ω]	Q_3 [$10^{-6} \text{ F s}^{b-1}$]	b	R_3 [Ω]
Spin-coated device	10	0.381	0.979	178	0.15	0.808	254
Spray-coated device	11	0.235	0.850	191	0.831	0.806	367

stability, and nontoxicity. In this study, we report for the first time spray process for the deposition of highly processable $\text{Cs}_2\text{AgBiBr}_6$ double perovskite thin films. Ultrasonic spray-coating allows for the deposition of very smooth and uniform thin films, with smaller and better connected grains in comparison with the spin-coated benchmark. In addition to microstructural improvements, spray-coated films show more suitable light absorption properties than the spin-coated ones. The further incorporation of the spray-coated $\text{Cs}_2\text{AgBiBr}_6$ double perovskite thin films in full devices leads to a 2.3% photoconversion efficiency, which is one of the highest values for spin-coated benchmarks. Such beneficial effect is directly correlated to the improvement of the $\text{Cs}_2\text{AgBiBr}_6$ interface induced by the spray-coating process. Indeed, from EIS data, spray-coated devices show lower interfacial recombination rates than spin-coated ones. As a consequence of the interface optimization, spray-coated devices lead to an impressively high V_{oc} of 1.09 V compared with 0.82 V for the spin-coated benchmark, and slightly surpassing the V_{oc} reached by a solution-processed $\text{Cs}_2\text{AgBiBr}_6$ double perovskite layer with additional interface optimization by dye interlayer engineering. However, further work will be needed to ensure better infiltration of the spray-coated analogue into the mesoporous electrodes and expect to surpass spin-coated electrodes. This study motivates strong interest in ultrasonic spray deposition for the optimization of $\text{Cs}_2\text{AgBiBr}_6$ solar cells in terms of light absorption properties and charge transfer at the $\text{Cs}_2\text{AgBiBr}_6$ /Spiro-OMeTAD interface. Most importantly, this deposition method can be adapted for the development of large-area solar cells devices and promote the scaled commercialization of perovskite-like solar cell technologies, without losing conversion efficiency.

4. Experimental Section

Materials and Chemicals: Fluorine-doped tin oxide (FTO) covered glass of 2.2 mm thickness and $15 \Omega \text{sq}^{-1}$ sheet resistance (TEC15, Greatcell Solar) were used as substrates. Following chemicals were purchased from various commercial suppliers: chlorhydric acid HCl (VWR, 37%), metallic zinc powder (Roth, $\geq 98\%$), titanium diisopropoxide bis(acetylacetonate) (TAA) (Sigma-Aldrich, 75 wt% in isopropanol), anhydrous ethanol EtOH (Acros, 99.5%), TiO_2 nanoparticle paste (Greatcell Solar 18NR-T), titanium chloride (TiCl_4) (Merck, $\geq 97.0\%$), cesium bromide (Alfa Aesar, $\geq 99.9\%$), bismuth bromide (Alfa Aesar, $\geq 99.0\%$), silver bromide (VWR, $\geq 99.5\%$), DMSO (Sigma-Aldrich, $>99.9\%$), N,N' -dimethylformamide (DMF) (Acros Organic, 99.9%), anhydrous chlorobenzene (Sigma-Aldrich, 99.8%), 2,2',7,7'-Tetrakis-9,9'-spirobifluorene Spiro-OMeTAD (Borun, $>99.9\%$), lithium bis(trifluoromethanesulfonyl)imide (Li-TFSI) (Sigma-Aldrich, 99.95%), 4-*tert*-butylpyridine (Sigma-Aldrich, 96%), and anhydrous *n*-butanol (*n*-BuOH) (Fischer, $>99.8\%$).

Substrate Preparation: First, FTO-glass substrates were cut into $2.0 \times 2.0 \text{ cm}^2$ pieces and etched with HCl (2 M) and metallic zinc powder to strip parts of the FTO and prevent short circuits in the final PV cell. Substrates were cleaned over three consecutive washing steps (with soap, ethanol, and acetone, respectively) under ultrasonication before being dried under air.

A compact hole blocking layer of TiO_2 (c- TiO_2 , $\sim 30 \text{ nm}$ thick) was then deposited by ultrasonic spray pyrolysis of TAA (2.2 mL) in ethanol (30.0 mL) solution from a Sono-Tek Exactacoat system combined with an Accumist nozzle. The following spraying parameters were used: stall power of 3.5 W, oxygen carrier gas flow of 0.9 psi, flow rate of 0.25 mL min^{-1} , nozzle speed of 100 mm s^{-1} , area spacing of 4 mm, nozzle-to-substrate distance of 5.5 cm, and substrate temperature of 450°C .

The deposition pattern was repeated three times so to obtain a 30 nm-thick TiO_2 film. Finally, a thermal treatment at 500°C (ramp 100°C h^{-1}) was performed for 30 min to crystallize TiO_2 in form of anatase phase. After a cleaning treatment under UV-ozone for 15 min, a 150 nm-thick mesoporous (mp)- TiO_2 layer was deposited onto the c- TiO_2 layer. Commercial TiO_2 nanoparticle paste (Greatcell Solar 18NR-T) was diluted in absolute ethanol (1:9.8 weight ratio) and spin-coated at 1500 rpm for 30 s, followed by subsequent annealing at 500°C (ramp 100°C h^{-1}) for 30 min. The mp- TiO_2 layer was immersed in an aqueous TiCl_4 solution ($4 \times 10^{-2} \text{ M}$) for 30 min at 60°C to allow further improvement of the connectivity between the TiO_2 nanoparticles. Then, samples were successively rinsed with water and EtOH, dried with compressed air and then calcined for 30 min at 450°C in a preheated oven. Before the double perovskite film deposition, a final cleaning treatment under UV ozone for 15 min was applied to the samples.

Double Perovskite Preparation Spin-Coating: A 0.30 M $\text{Cs}_2\text{AgBiBr}_6$ solution was prepared by mixing 134.6 mg of BiBr_3 , 56.3 mg of AgBr, and 127.7 mg CsBr in 1 mL of DMSO in an argon-filled glove box. Then, the solution was preheated at 75°C to allow the complete dissolution of the precursors. Before spin-coating, both the solution and the substrate were preheated at 70°C . The hot precursor solution (150 μL) was spin-coated onto the mp- TiO_2 /c- TiO_2 /FTO glass substrates at 2000 rpm for 30 s. The sample was then annealed at 285°C for 5 min under argon atmosphere to allow the formation of the desired double perovskite crystal phase (Figure 7).

Ultrasonic Spray-Coating: A 0.15 M $\text{Cs}_2\text{AgBiBr}_6$ solution was prepared by mixing 1009.5 mg of BiBr_3 , 422.4 mg of AgBr, and 957.6 mg CsBr in 15 mL of DMF:DMSO (4:1 volume). The solution concentration has been optimized to prepare samples with the same thickness compared with the spin-coated counterparts.^[36] Noteworthy, the concentration lowering by switching from spin-coating to spray-coating was implemented so to adapt to the reduction of materials loss in spray deposition compared with spin-coating process. The solution was stirred at 80°C overnight and was then filtered with a $0.45 \mu\text{m}$ micropore filter. As for the spray-coating of the c- TiO_2 layer, the ultrasonic spray-coating of the double perovskite films was performed with a Sono-Tek Exactacoat system combined with an Accumist nozzle. The following spraying parameters were used: stall power of 3.5 W, air carrier gas flow at 0.9 psi, flow rate of 0.25 mL min^{-1} , nozzle speed of 80 mm s^{-1} , area spacing of 4 mm, single pass, nozzle-to-substrate distance of 6.5 cm, and substrate temperature of 150°C . The sprayed films were finally annealed at 285°C for 5 min.

Solar Cell Fabrication: First, Spiro-OMeTAD (186 mg) and an additive solution (84 μL)—from 0.175 g Li-TFSI and 312.5 μL of *tert*-butylpyridine in 1 mL of anhydrous butanol—were mixed with anhydrous chlorobenzene (2 mL). The solution was then deposited by spin-coating at 2000 rpm for 60 s. After having scratched off the TiO_2 /double perovskite/Spiro-OMeTAD layers from the photoanode contact, a gold counter-electrode layer was deposited by thermal evaporation (home-made apparatus) using a patterned mask (Figure S1 and S2, Supporting Information).

Characterization: A field emission gun microscope ESEM XL30 (FEI) under a 15 kV accelerating voltage and high vacuum was used for the morphological characterization of individual layers and assembled cells by SEM. All samples were coated with gold before characterization.

A Bruker D8 grazing incidence diffractometer with Cu K α radiation was used for XRD characterization of the crystallized materials.

A Shimadzu 3600 Plus instrument with an integrating sphere (ISR-1503) was used for optical measurements by UV-vis-NIR spectrometry.

A class A solar simulator (Newport Spectra Physics) coupled to a Keithley 2400 sourcemeter measured the PV conversion efficiency of the cells (average on 20 devices). Calibration was performed using a KG5 filtered silicon reference solar cell from Newport. Photocurrent density versus applied voltage curves (J - V curves) were measured on $2.0 \times 2.0 \text{ cm}^2$ double perovskite devices under simulated 1 sun illumination (filter AM1.5) at room temperature, using a black mask with a 0.0355 cm^2 aperture. Forward (0–1.2 V) and backward (1.2–0 V) measurements were performed with an increment of 4 mV (0.2 s/step).

For the EIS, data were collected using a BioLogic SP-200 potentiostat (Science Instrument) and analyzed with the EC-Lab software. A sinusoidal potential perturbation was applied on the assembled devices and the

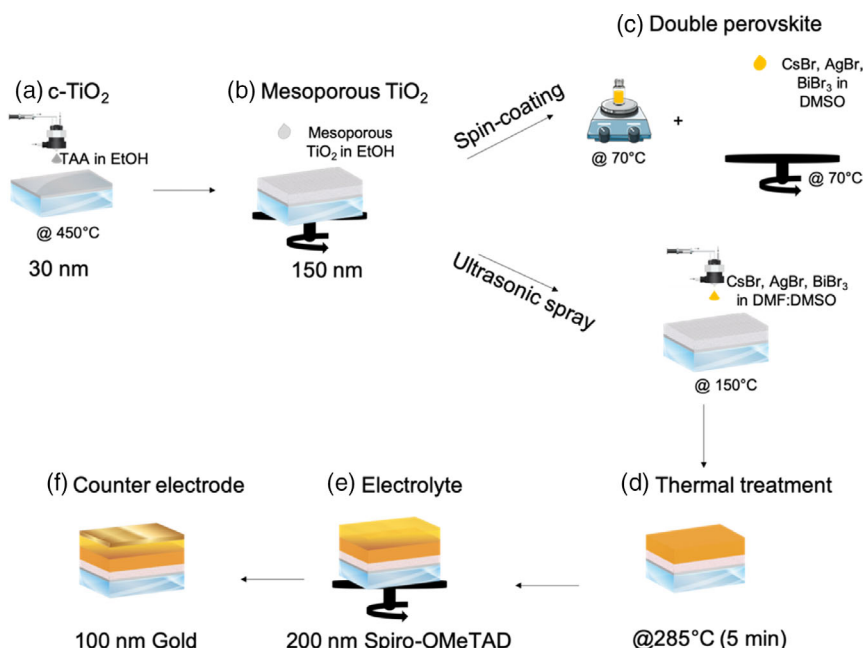


Figure 7. Overview of the manufacturing process of the $\text{Cs}_2\text{AgBiBr}_6$ -based solar cells.

current variation response was recorded. A frequency range of 3–85 MHz with 10 mV sinusoidal modulation was applied for the EIS data acquisition for the spray-coated and spin-coated devices. Measurements were performed at room temperature under standard 1 sun illumination (AM1.5 filter) and in open-circuit potential (OCP) conditions.

The PL maps were acquired using a wide-field, hyperspectral imaging microscope (Photon etc. IMA VIS), equipped with a $20\times$ or $100\times$ objective, and detected with a front-illuminated, low-noise CCD camera. A continuous wave (CW), power-tunable 405 nm laser was used as the PL excitation source with an incident photon flux of 9×10^{20} or 9×10^{21} photons $\text{m}^{-2} \text{s}^{-1}$. These values correspond well to the generation rate under 1 or 10 suns of $n_{1\text{sun}} = \int_{350\text{nm}}^{630\text{nm}} \text{AM1.5}G(\lambda) = 9 \times 10^{20} \text{ m}^{-2} \text{s}^{-1}$. All data were acquired in ambient atmospheric conditions.

Time-resolved PL spectra were recorded using a confocal single-photon counting fluorescence microscope from Picoquant. Excitation was performed at $\lambda = 405 \text{ nm}$ using a $20\times$ air objective at an intensity of $1.3 \mu\text{J cm}^{-2}$ for each pulse using a repetition rate of 0.25 MHz. The PL was collected through a dichroic mirror by a $\lambda = 450 \text{ nm}$ long-pass filter onto a single-photon counting Single Photon Avalanche Diode detector.

EQE spectra were recorded under N_2 atmosphere using a 100 W halogen lamp, mechanically chopped at 80 Hz and a double monochromator as light source, coupled into an optical fiber. Calibration was performed using an UV-enhanced Si photodetector (Newport). The photogenerated current was measured using a lock-in-amplifier from Stanford Research.

Supporting Information

Supporting Information is available from the Wiley Online Library or from the author.

Acknowledgements

This work was supported by the Department of Chemistry of the University of Liege and by Région Wallonne (SOLIDYE_1 Project, Complement FEDER, grant agreement no. 1510607). The authors acknowledge fellow team members of GREENMAT for additional technical and administrative

support. A.M., J.D., and G.S. thank Région Wallonne (SOLIDYE_1 Project, Complement FEDER, Grant agreement 1510607). F.L. acknowledges financial support from the Alexander von Humboldt Foundation via the Feodor Lynen program. S.D.S. acknowledges the Royal Society and Tata Group (UF150033). The authors acknowledge the EPSRC for funding (EP/R023980/1). This project has received funding from the European Union's Horizon 2020 research and innovation program under the Marie Skłodowska-Curie grant agreement no. 841265.

Conflict of Interest

The authors declare no conflict of interest.

Data Availability Statement

The data that support the findings of this study are available from the corresponding author upon reasonable request.

Keywords

$\text{Cs}_2\text{AgBiBr}_6$ double perovskites, lead-free solar cells, thin films, ultrasonic spray deposition

Received: June 16, 2021

Revised: July 9, 2021

Published online:

- [1] S. D. Stranks, G. E. Eperon, G. Grancini, C. Menelaou, M. J. P. Alcocer, T. Leijtens, L. M. Herz, A. Petrozza, H. J. Snaith, *Science* **2013**, 342, 341.
- [2] C. S. Ponseca Jr., T. J. Savenije, M. Abdellah, K. Zheng, A. Yartsev, T. Pascher, T. Harlang, P. Chabera, T. Pullerits, A. Stepanov, J. Wolf, V. Sundström, *J. Am. Chem. Soc.* **2014**, 136, 5189.

- [3] G. Xing, N. Mathews, S. S. Lim, Y. M. Lam, S. Mhaisalkar, T. C. Sum, *Science* **2013**, 342, 344.
- [4] C. C. Stoumpos, C. D. Malliakas, M. G. Kanatzidis, *Inorg. Chem.* **2013**, 52, 9019.
- [5] Best Research-Cell Efficiency Chart, <https://www.nrel.gov/pv/cell-efficiency.html> (accessed: February 2021).
- [6] M. M. Lee, J. Teuscher, T. Miyasaka, T. N. Murakami, H. J. Snaith, *Science* **2012**, 338, 643.
- [7] J. Li, H.-L. Cao, W.-B. Jiao, Q. Wang, M. Wei, I. Cantone, J. Lü, A. Abate, *Nat. Commun.* **2020**, 310, 1.
- [8] A. Babayigit, A. Ethirajan, M. Muller, B. Conings, *Nat. Publ. Gr.* **2016**, 15, 247.
- [9] M. Lyu, J.-H. Yun, P. Chen, M. Hao, L. Wang, *Adv. Energy Mater.* **2017**, 7, 1602512.
- [10] R. Nie, R. R. Sumukam, S. H. Reddy, M. Banavoth, S. Il Seok, *Energy Environ. Sci.* **2020**, 13, 2363.
- [11] M. Palummo, D. Varsano, E. Berrios, K. Yamashita, G. Giorgi, *Energies* **2020**, 13, 1.
- [12] X. Yang, W. Wang, R. Ran, W. Zhou, Z. Shao, *Energy Fuels* **2020**, 34, 10513.
- [13] L. Liang, P. Gao, *Adv. Sci.* **2018**, 1700331, 1.
- [14] Q. Zhang, F. Hao, J. Li, Y. Zhou, Y. Wei, H. Lin, *Sci. Technol. Adv. Mater.* **2018**, 6996, 1.
- [15] Z. Xiao, Z. Song, Y. Yan, *Adv. Matter.* **2019**, 1803792, 1.
- [16] F. Igbari, R. Wang, Z. Wang, X. Ma, Q. Wang, K. Wang, *Nano Lett.* **2019**, 19, 1.
- [17] W. Ning, F. Wang, B. Wu, J. Lu, Z. Yan, X. Liu, Y. Tao, J.-M. Liu, W. Huang, M. Fahlman, L. Hultman, T. C. Sum, F. Gao, *Adv. Mater.* **2018**, 30, 1.
- [18] W. Gao, C. Ran, J. Xi, B. Jiao, W. Zhang, M. Wu, X. Hou, Z. Wu, *ChemPhysChem* **2018**, 19, 1696.
- [19] C. Wu, Q. Zhang, Y. Liu, W. Luo, X. Guo, Z. Huang, H. Ting, W. Sun, X. Zhong, S. Wei, S. Wang, Z. Chen, L. Xiao, *Adv. Sci.* **2018**, 1700759, 2.
- [20] M. Pantaler, K. T. Cho, V. I. E. Queloz, I. G. Benito, C. Fettkenhauer, I. Anusca, M. K. Nazeeruddin, D. C. Lupascu, G. Grancini, *ACS Energy Lett.* **2018**, 3, 1.
- [21] E. Greul, M. L. Petrus, A. Binek, P. Docampo, T. Bein, *J. Mater. Chem. A* **2017**, 5, 19972.
- [22] M. Ghasemi, L. Zhang, J.-H. Yun, M. Hao, D. He, P. Chen, Y. Bai, T. Lin, M. Xiao, A. Du, M. Lyu, L. Wang, *Adv. Funct. Mater.* **2020**, 2002342, 1.
- [23] J. Li, J. Duan, X. Yang, Y. Duan, P. Yang, Q. Tang, *Adv. Funct. Mater.* **2020**, 2001557, 1.
- [24] B. Wang, L. Yang, C. Dall'Agnese, A. Jena, S. Sasaki, T. Miyasaka, H. Tamiaki, X. Wang, *Sol. RRL* **2020**, 4, 2.
- [25] M. Wang, P. Zeng, S. Bai, J. Gu, F. Li, Z. Yang, M. Liu, *Sol. RRL* **2018**, 2, 1.
- [26] N. Pai, J. Lu, M. Wang, A. S. R. Chesman, A. Seeber, P. V. Cherepanov, D. C. Senevirathna, T. R. Gengenbach, N. V. Medhekar, P. C. Andrews, U. Bach, A. N. Simonov, *J. Mater. Chem. A* **2020**, 8, 2008.
- [27] P. Fan, H. Peng, Z. Zheng, Z. Chen, S. Tan, X. Chen, *Nanomaterials* **2019**, 6, 1.
- [28] Z. Zhang, C. Wu, D. Wang, G. Liu, Q. Zhang, W. Luo, X. Qi, X. Guo, Y. Zhang, Y. Lao, B. Qu, L. Xiao, Z. Chen, *Org. Electron.* **2019**, 74, 204.
- [29] F. Igbari, Z. K. Wang, L. S. Liao, *Adv. Energy Mater.* **2019**, 9, 1.
- [30] Z. Li, P. Wang, C. Ma, F. Igbari, Y. Kang, K.-L. Wang, W. Song, C. Dong, Y. Li, J. Yao, D. Meng, Z.-K. Wang, Y. Yang, *J. Am. Chem. Soc.* **2021**, 143, 2593.
- [31] M. T. Höranter, T. Leijtens, M. E. Ziffer, G. E. Eperon, M. G. Christoforo, M. D. McGehee, H. J. Snaith, *ACS Energy Lett.* **2017**, 2, 2506.
- [32] G. Volonakis, M. R. Filip, A. A. Haghighirad, N. Sakai, B. Wenger, H. J. Snaith, F. Giustino, *J. Phys. Chem. Lett.* **2016**, 7, 1254.
- [33] A. H. Slavney, T. Hu, A. M. Lindenberg, H. I. Karunadasa, *J. Am. Chem. Soc.* **2016**, 138(7), 2138.
- [34] Y. Deng, X. Zheng, Y. Bai, Q. Wang, J. Zhao, J. Huang, *Nat. Energy* **2018**, 3, 560.
- [35] J. E. Bishop, C. D. Read, J. A. Smith, T. J. Routledge, D. G. Lidzey, *Sci. Rep.* **2020**, 6610, 1.
- [36] C. N. Savory, A. Walsh, D. O. Scanlon, *ACS Energy Lett.* **2016**, 1, 949.
- [37] L. Schade, S. Mahesh, G. Volonakis, M. Zacharias, B. Wenger, F. Schmidt, S. Vajjala Kesava, D. Prabhakaran, M. Abdijalebi, M. Lenz, F. Giustino, G. Longo, P. G. Radaelli, H. J. Snaith, *ACS Energy Lett.* **2021**, 6, 1073.
- [38] A. Dey, A. F. Richter, T. Debnath, H. Huang, L. Polavarapu, J. Feldmann, *ACS Nano* **2020**, 14, 5855.
- [39] S. J. Zelewski, J. M. Urban, A. Surrente, D. K. Maude, A. Kuc, L. Schade, R. D. Johnson, M. Dollmann, P. K. Nayak, H. J. Snaith, P. Radaelli, R. Kudrawiec, R. J. Nicholas, P. Plochocka, M. Baranowski, *J. Mater. Chem. C* **2019**, 7, 8350.
- [40] A. H. Slavney, T. Hu, A. M. H. I. Lindenberg, H. I. Karunadasa, *J. Am. Chem. Soc.* **2017**, 2, 3.
- [41] A. Maho, M. Lobet, N. Daem, P. Piron, G. Spronck, J. Loicq, R. Cloots, P. Colson, C. Henrist, J. Dewalque, *ACS Appl. Energy Mater.* **2021**, 4, 1108.
- [42] W. Tress, K. Leo, M. Riede, *Phys. Rev. B: Condens. Matter Mater. Phys.* **2012**, 85, 1.